 CMES, vol.72, no.4, pp.299-334, 2011

A C^2-Continuous Control-Volume Technique Based on Cartesian Grids and Two-Node Integrated-RBF Elements for Second-Order Elliptic Problems

D.-A. An-Vo[1], N. Mai-Duy[1] and T. Tran-Cong[1]

Abstract: This paper presents a new control-volume discretisation method, based on Cartesian grids and integrated-radial-basis-function elements (IRBFEs), for the solution of second-order elliptic problems in one and two dimensions. The governing equation is discretised by means of the control-volume formulation and the division of the problem domain into non-overlapping control volumes is based on a Cartesian grid. Salient features of the present method include (i) an element is defined by two adjacent nodes on a grid line, (ii) the IRBF approximations on each element are constructed using only two RBF centres (a smallest RBF set) associated with the two nodes of the element and (iii) the IRBFE solution is C^2-continuous across the interface between two adjacent elements. The first feature guarantees consistency of the flux at control-volume faces. The second feature helps represent curved profiles between 2 adjacent nodes and leads to a sparse and banded system matrix, facilitating the employment of a large number of nodes. The third feature enhances the smoothness of element-based solutions, allowing a better estimation for the physical quantities involving derivatives. Numerical results indicate that (i) the proposed method can work with a wide range of the shape-parameter/RBF-width and (ii) the proposed technique yields more accurate results and faster convergence, especially for the approximation of derivatives, than the standard control-volume technique.

Keywords: integrated-radial-basis-function element, Cartesian grid, control-volume formulation, local approximation, second-order elliptic problem, C^2-continuous solution.

[1] Computational Engineering and Science Research Centre, Faculty of Engineering and Surveying, The University of Southern Queensland, Toowoomba, QLD 4350, Australia

1 Introduction

Traditional techniques used for solving second-order elliptic differential equations include overlapping finite difference methods (FDMs), non-overlapping finite element methods (FEMs), boundary element methods (BEMs) and control volume methods (CVMs). These methods typically utilise polynomials as an interpolator. To avoid notorious polynomial snaking phenomena, low-order polynomials such as linear variations are widely used, usually leading to errors of order h^2, where h is the mesh spacing. For element-based solutions, only the approximating function (not its partial derivatives) is continuous across elements (i.e. C^0 continuity). The overall error can be reduced by using progressively denser meshes. A mesh needs be sufficiently fine to mitigate the effects of discontinuity of partial derivatives. It is thus desirable to have discretisation methods that can produce a solution of higher-order continuity across elements.

Radial basis functions (RBFs) have successfully been used for the approximation of scattered data over the last several decades. They have also emerged as an attractive scheme for the numerical solution of ordinary and partial differential equations (ODEs and PDEs) (e.g. Fasshauer (2007) and references therein). Theoretically, some RBF-based methods can be as competitive as spectral methods; the two types of methods can exhibit spectral accuracy. Unlike pseudo-spectral techniques, they do not require the use of tensor products in constructing the approximations in two dimensions or more. The RBF approximations usually rely on a set of distinct points rather than a set of small elements. When this characteristic is combined with the point-collocation formulation, the resultant discretisation methods are truly meshless (e.g. Kansa (1990)). RBF-based collocation methods can be applied to differential problems defined on irregular domains without added difficulties. Apart from point-collocation, RBFs have also been employed as trial functions in other formulations such as the Galerkin, subregion collocation and inverse statements, resulting in enhanced rates of convergence ($O(h^\alpha)$ with $\alpha > 2$) of these approaches. Works in this research trend include Atluri, Han, and Rajendran (2004); Sellountos and Sequeira (2008); Orsini, Power, and Morvan (2008); Mohammadi (2008).

In a pivotal paper on function approximation by Franke (1982), it was pointed out that the multiquadric (MQ) RBF scheme yields the most accurate results. The present work employs the MQ whose form is defined by

$$g_i(\mathbf{x}) = \sqrt{(\mathbf{x}-\mathbf{c}_i)^2 + a_i^2}, \tag{1}$$

where $\mathbf{c}_i$ and a_i are the centre and the shape parameter of the ith MQ, respectively. A set of interpolation points is taken to be a set of RBF centres. In Mai-Duy and

Tran-Cong (2003), the value of the shape parameter was simply chosen as $a_i = \beta h_i$ with β being a given positive number and h_i the distance between $\mathbf{c}_i$ and its nearest neighbour. When the direct way of computing the interpolants is used, RBF-based methods such as those using MQs are known to suffer from the so-called uncertainty principle. As the value of β increases, the error reduces while the matrix condition number increases undesirably. In practice, one desires to use large βs up to a value at which the system matrix is still in good condition. RBF-based methods can be classified into two categories: global and local. Global methods use every RBF on the whole domain to construct the approximations at a point, resulting in a fully populated system matrix (c.f. Kansa (1990); Sarler (2005); Zerroukat, Power, and Chen (1998); Mai-Duy and Tran-Cong (2001)). When the number of RBF centres and/or the value of β increase, the condition of RBF matrices deteriorates rapidly. Such drawbacks typically render global methods unsuitable for complex problems, where many points are required for a proper simulation. In addition, β to be used is confined to small values. For local methods (e.g. Tolstykh and Shirobokov (2003); Shu, Ding, and Yeo (2003); Lee, Liu, and Fan (2003); Šarler and Vertnik (2006); Divo and Kassab (2007); Sanyasiraju and Chandhini (2008); Mai-Duy and Tran-Cong (2009)), only a few RBFs are activated for the approximations at a point. The resultant system matrix is sparse and banded, which is suitable for handling large-scale problems. However, trade-offs include the loss of spectral accuracy and high-order continuity of the approximate solution. Various schemes have been proposed to enhance the performance of local methods. Using large values of β appears to be an economical and effective way (Cheng, Golberg, Kansa, and Zammito (2003)). In the case of non-overlapping domain-decompositions, where a large problem is replaced with a set of sub-problems of much smaller sizes, the computed solution is only a C^1 function across the subdomain interfaces (Li and Hon (2004)). It is noted that errors of RBF solutions are larger near interfaces/boundaries (Fedoseyev, Friedman, and Kansa (2002)) and with Neumann boundary conditions than with Dirichlet boundary conditions (Libre, Emdadi, Kansa, Rahimian, and Shekarchi (2008)).

In a conventional RBF scheme (Kansa (1990)), the original function is decomposed into RBFs and its derivatives are then obtained through differentiation. Some RBF schemes such as those based on MQs are known to possess spectral accuracy with errors in the $O(\lambda^\chi)$, where $0 < \lambda < 1$. Through numerical experiment, for a certain range of a, Cheng, Golberg, Kansa, and Zammito (2003) established the error estimate as $O(\lambda^{\sqrt{a}/h})$. In the approximation of kth derivative, Madych (1992) showed that the convergence rate is reduced to $O(\lambda^{\chi-k})$. To avoid such reduction of convergence rate caused by differentiation in a conventional scheme, Mai-Duy and Tran-Cong (2003) proposed an indirect or integral approach. RBFs were used to

represent highest order derivatives and such RBF-based approximants are then integrated to yield expressions for lower-order derivatives and eventually the function itself. This approach is less sensitive to noise than the usual differential approach and appears to be more suitable for applications involving derivatives such as the numerical solution of ODEs and PDEs. Recently, towards the analysis of large-scale problems, a numerical scheme, based on one-dimensional integrated RBFs (1D-IRBFs), point collocation and Cartesian grids, was reported in Mai-Duy and Tran-Cong (2007). In this scheme, the 1D-IRBF approximations at a grid point $\mathbf{x}$ only involve nodal points that lie on grid lines crossing at $\mathbf{x}$ rather than the whole set of nodal points, leading to a considerable saving of computing time and memory space over the original IRBF schemes (e.g. Mai-Duy, Le-Cao, and Tran-Cong (2008); Le-Cao, Mai-Duy, and Tran-Cong (2009); Ho-Minh, Mai-Duy, and Tran-Cong (2009); Ngo-Cong, Mai-Duy, Karunasena, and Tran-Cong (2011)).

In the present work, the problem domain, which can be rectangular or non-rectangular, is represented by a Cartesian grid. Each grid node is associated with a control volume (CV) of rectangular shape. To estimate the values of the flux at the middle points on the interfaces, the approximations for the field variable and its derivatives are constructed using IRBFs over elements defined by two adjacent grid nodes. Unlike our previous work, e.g. Mai-Duy and Tran-Cong (2010), 1D-IRBFs are implemented here with two RBF centres only and the approximations are non-overlapping. Furthermore, the constants of integration are exploited to impose continuity of second-order derivatives across two adjacent elements. It can be seen that the use of two RBFs (a smallest RBF set) allows a wide range of β to be used and leads to sparse system matrices. To enhance accuracy, one can thus increase the value of β and/or the number of RBFs. Continuity of the approximate solution, its first and second-order derivatives across two adjacent IRBF elements (or simply across elements for brevity in the remaining discussion) is guaranteed in the proposed technique.

An outline of the paper is as follows. In Section 2, a brief review of IRBFs including 1D-IRBFs is given. In Section 3, the proposed C^2-CV technique based on 2-node IRBFEs for second-order elliptic differential problems is presented. In Section 4, the proposed technique is validated through function approximation and solution of ODEs and PDEs. Section 5 concludes the paper.

2 Brief review of integrated RBFs

The indirect/integral RBF approach consists in decomposing highest-order derivatives under consideration into RBFs and then integrating these RBFs to yield expressions for lower-order derivatives and finally the original function itself (Mai-Duy and Tran-Cong (2003)). In the case of second-order PDEs in two dimensions,

integrated MQ expressions are given by

$$\frac{\partial^2\phi}{\partial\eta^2}(\mathbf{x}) = \sum_{i=1}^{n} w_i \sqrt{(\mathbf{x}-\mathbf{c}_i)^2 + a_i^2} = \sum_{i=1}^{n} w_i I_i^{(2)}(\mathbf{x}), \qquad \mathbf{x} \in \Omega, \tag{2}$$

$$\frac{\partial\phi}{\partial\eta}(\mathbf{x}) = \sum_{i=1}^{n} w_i I_i^{(1)}(\mathbf{x}) + C_1(\theta), \tag{3}$$

$$\phi(\mathbf{x}) = \sum_{i=1}^{n} w_i I_i^{(0)}(\mathbf{x}) + C_1(\theta)\eta + C_2(\theta), \tag{4}$$

where Ω is the domain of interest, ϕ a function, η a component of $\mathbf{x}$, n the number of RBFs, $\{w_i\}_{i=1}^n$ the set of RBF weights, $C_1(\theta)$ and $C_2(\theta)$ the constants of integration which are functions of θ ($\theta \neq \eta$), $I_i^{(2)}(\mathbf{x})$ conveniently denotes the MQ, $I_i^{(1)}(\mathbf{x}) = \int I_i^{(2)}(\mathbf{x})d\eta$, and $I_i^{(0)}(\mathbf{x}) = \int I_i^{(1)}(\mathbf{x})d\eta$. Explicit forms of $I_i^{(1)}(\mathbf{x})$ and $I_i^{(0)}(\mathbf{x})$ can be found in Mai-Duy and Tran-Cong (2001).

When the analysis domain Ω is a line segment, expressions (2), (3) and (4) reduce to

$$\frac{d^2\phi}{d\eta^2}(\eta) = \sum_{i=1}^{n} w_i \sqrt{(\eta-c_i)^2 + a_i^2} = \sum_{i=1}^{n} w_i I_i^{(2)}(\eta), \tag{5}$$

$$\frac{d\phi}{d\eta}(\eta) = \sum_{i=1}^{n} w_i I_i^{(1)}(\eta) + C_1, \tag{6}$$

$$\phi(\eta) = \sum_{i=1}^{n} w_i I_i^{(0)}(\eta) + C_1\eta + C_2, \tag{7}$$

where C_1 and C_2 are simply constant values.

Expressions (5), (6) and (7), called 1D-IRBFs, can also be used in conjunction with Cartesian grids for solving 2D problems. Advantages of 1D-IRBFs over 2D-IRBFs are that they possess some "local" properties and are constructed with a much lower cost. However, numerical experiments show that 1D-IRBFs still cannot work with large values of β. In the present work, 1D-IRBF-based schemes are further localised.

3 Proposed C^2-continuous control-volume technique

The problem domain is embedded in a Cartesian grid. In the case of non-rectangular domains, we remove grid points outside the problem domain. Grid points inside the problem domain are taken to be interior nodes, while boundary nodes are defined as the intersection of the grid lines and the boundaries. Generally, each nodal point is associated with a control volume, over which the differential equation is directly

integrated. For illustrative purposes, the proposed technique is presented for the following 2D PDE

$$\frac{\partial^2 \phi}{\partial x^2} + \frac{\partial^2 \phi}{\partial y^2} = b(x,y), \tag{8}$$

where $b(x,y)$ is some prescribed function. Following the work of Patankar (1980), (8) is transformed into a set of discretised equations. A distinguishing feature of the proposed technique is that the approximations used for the flux estimation at the interfaces are based on 1D-IRBFs rather than linear polynomials. In our previous work Mai-Duy and Tran-Cong (2010), 1D-IRBFs were implemented using every node on a grid line. In contrast, the present 1D-IRBFs are constructed locally over straight-line segments between two adjacent nodal points only, called 2-node IRBF elements (IRBFEs). There are two types of elements, namely interior and semi-interior IRBFEs. An interior element is formed using two adjacent interior nodes while a semi-interior element is generated by an interior node and a boundary node. In the remainder of this section, 1D-IRBFs are first utilised to represent the variation of the field variable and its derivatives on interior and semi-interior elements, and IRBFEs are then incorporated into the CV formulation. It will be shown that the approximate solution is a C^2 function across IRBFEs.

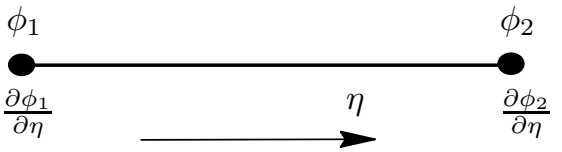

Figure 1: Schematic outline for 2-node IRBFE.

3.1 Interior elements

1D-IRBF expressions for interior elements are of similar forms. Consider an interior element, $\eta \in [\eta_1, \eta_2]$, and its two nodes are locally named as 1 and 2. Let $\phi(\eta)$ be a function and ϕ_1, $\partial\phi_1/\partial\eta$, ϕ_2 and $\partial\phi_2/\partial\eta$ be the values of ϕ and $d\phi/d\eta$ at the two nodes, respectively (Fig. 1). The 2-node IRBFE scheme approximates

$\phi(\eta)$ using two MQs whose centres are located at η_1 and η_2. Expressions (5), (6) and (7) become

$$\frac{\partial^2\phi}{\partial\eta^2}(\eta) = w_1\sqrt{(\eta-c_1)^2+a_1^2} + w_2\sqrt{(\eta-c_2)^2+a_2^2} = w_1 I_1^{(2)}(\eta) + w_2 I_2^{(2)}(\eta), \tag{9}$$

$$\frac{\partial\phi}{\partial\eta}(\eta) = w_1 I_1^{(1)}(\eta) + w_2 I_2^{(1)}(\eta) + C_1, \tag{10}$$

$$\phi(\eta) = w_1 I_1^{(0)}(\eta) + w_2 I_2^{(0)}(\eta) + C_1\eta + C_2, \tag{11}$$

where $I_i^{(1)}(\eta) = \int I_i^{(2)}(\eta)d\eta$, $I_i^{(0)}(\eta) = \int I_i^{(1)}(\eta)d\eta$ with $i = (1,2)$, and C_1 and C_2 are the constants of integration. By collocating (11) and (10) at η_1 and η_2, the relation between the physical space and the RBF coefficient space is obtained

$$\underbrace{\begin{pmatrix} \phi_1 \\ \phi_2 \\ \frac{\partial\phi_1}{\partial\eta} \\ \frac{\partial\phi_2}{\partial\eta} \end{pmatrix}}_{\widehat{\psi}} = \underbrace{\begin{pmatrix} I_1^{(0)}(\eta_1) & I_2^{(0)}(\eta_1) & \eta_1 & 1 \\ I_1^{(0)}(\eta_2) & I_2^{(0)}(\eta_2) & \eta_2 & 1 \\ I_1^{(1)}(\eta_1) & I_2^{(1)}(\eta_1) & 1 & 0 \\ I_1^{(1)}(\eta_2) & I_2^{(1)}(\eta_2) & 1 & 0 \end{pmatrix}}_{\mathscr{I}} \underbrace{\begin{pmatrix} w_1 \\ w_2 \\ C_1 \\ C_2 \end{pmatrix}}_{\widehat{w}}, \tag{12}$$

where $\widehat{\psi}$ is the nodal-value vector, $\mathscr{I}$ the conversion matrix, and $\widehat{w}$ the coefficient vector. It is noted that not only the nodal values of ϕ but also of $\partial\phi/\partial\eta$ are incorporated into the conversion system and this imposition is done in an exact manner owing to the presence of integration constants. Solving (12) yields

$$\widehat{w} = \mathscr{I}^{-1}\widehat{\psi}. \tag{13}$$

Substitution of (13) into (11), (10) and (9) leads to

$$\phi(\eta) = \left[I_1^{(0)}(\eta), I_2^{(0)}(\eta), \eta, 1\right]\mathscr{I}^{-1}\widehat{\psi}, \tag{14}$$

$$\frac{\partial\phi}{\partial\eta}(\eta) = \left[I_1^{(1)}(\eta), I_2^{(1)}(\eta), 1, 0\right]\mathscr{I}^{-1}\widehat{\psi}, \tag{15}$$

$$\frac{\partial^2\phi}{\partial\eta^2}(\eta) = \left[I_1^{(2)}(\eta), I_2^{(2)}(\eta), 0, 0\right]\mathscr{I}^{-1}\widehat{\psi}, \tag{16}$$

which allows one to express the values of ϕ and $\partial\phi/\partial\eta$ at any point η in $[\eta_1,\eta_2]$ in terms of four nodal unknowns, i.e. the values of the field variable and its first-order derivatives at the two extremes (also grid points) of the element.

3.2 Semi-interior elements

As mentioned earlier, a semi-interior element is defined by two nodes: an interior node and a boundary node. The subscripts 1 and 2 are now replaced with b (b represents a boundary node) and g (g an interior grid node), respectively. Experience shows that boundary treatments strongly affect the overall accuracy of a numerical solution. Thus several semi-interior elements for the Dirichlet-type and Neumann-type boundary conditions are proposed and investigated. Their construction processes are similar to that for interior elements, and therefore only the main differences are presented in the following sections.

3.2.1 Dirichlet boundary conditions

At η_b, the value of ϕ is given. We propose three types of semi-interior elements. The first one can work with problems with irregular geometries while the last two are limited to the case of 1D problems and 2D problems defined on rectangular domains. For 1D and rectangular domain cases, a boundary node is also a grid node and one can express the governing equation at that node in terms of one independent variable only, i.e. either $\eta \equiv x$ or $\eta \equiv y$. The last two types of semi-interior elements will take into account information on the governing equation at η_b.

Element IRBFE-D1: At $\eta = \eta_b$, this element uses information on ϕ only. The conversion system (12) reduces to

$$\begin{pmatrix} \phi_b \\ \phi_g \\ \frac{\partial \phi_g}{\partial \eta} \end{pmatrix} = \begin{pmatrix} I_b^{(0)}(\eta_b) & I_g^{(0)}(\eta_b) & \eta_b & 1 \\ I_b^{(0)}(\eta_g) & I_g^{(0)}(\eta_g) & \eta_g & 1 \\ I_b^{(1)}(\eta_g) & I_g^{(1)}(\eta_g) & 1 & 0 \end{pmatrix} \begin{pmatrix} w_b \\ w_g \\ C_1 \\ C_2 \end{pmatrix}. \tag{17}$$

It can be seen that the interpolation matrix for element *IRBFE-D1* is under-determined and its inverse can be obtained using the SVD technique (pseudo-inversion).

Element IRBFE-D2: At $\eta = \eta_b$, this element uses information on ϕ and the governing equation, which leads to the conversion system

$$\begin{pmatrix} \phi_b \\ \phi_g \\ \frac{\partial^2 \phi_b}{\partial \eta^2} \\ \frac{\partial \phi_g}{\partial \eta} \end{pmatrix} = \begin{pmatrix} I_b^{(0)}(\eta_b) & I_g^{(0)}(\eta_b) & \eta_b & 1 \\ I_b^{(0)}(\eta_g) & I_g^{(0)}(\eta_g) & \eta_g & 1 \\ I_b^{(2)}(\eta_b) & I_g^{(2)}(\eta_b) & 0 & 0 \\ I_b^{(1)}(\eta_g) & I_g^{(1)}(\eta_g) & 1 & 0 \end{pmatrix} \begin{pmatrix} w_b \\ w_g \\ C_1 \\ C_2 \end{pmatrix}. \tag{18}$$

In (18), $\partial^2 \phi_b / \partial \eta^2$ is a known value, obtained from the governing equation (8). For example, if η represents x, one has $\partial^2 \phi_b / \partial x^2 = b(x,y) - \partial^2 \phi_b / \partial y^2$ in which $\partial^2 \phi_b / \partial y^2$ is easily calculated from the given boundary condition ϕ on the vertical line $x = x_b$.

Element IRBFE-D3: At $\eta = \eta_b$, this element uses information on ϕ and $\partial\phi/\partial\eta$, resulting in the following system

$$\begin{pmatrix} \phi_b \\ \phi_g \\ \frac{\partial\phi_b}{\partial\eta} \\ \frac{\partial\phi_g}{\partial\eta} \end{pmatrix} = \begin{pmatrix} I_b^{(0)}(\eta_b) & I_g^{(0)}(\eta_b) & \eta_b & 1 \\ I_b^{(0)}(\eta_g) & I_g^{(0)}(\eta_g) & \eta_g & 1 \\ I_b^{(1)}(\eta_b) & I_g^{(1)}(\eta_b) & 1 & 0 \\ I_b^{(1)}(\eta_g) & I_g^{(1)}(\eta_g) & 1 & 0 \end{pmatrix} \begin{pmatrix} w_b \\ w_g \\ C_1 \\ C_2 \end{pmatrix}, \tag{19}$$

which has the same form as the interior element.

3.2.2 Neumann boundary conditions

In the context of Cartesian-grid-based methods, the implementation of a Neumann boundary condition still presents a great challenge. Special treatments, e.g. a boundary node does lie on a grid point, are required. Here, we restrict our attention to rectangular domains. At η_b, the value of $\partial\phi/\partial\eta$ is given. In the following, we propose two types of semi-interior elements.

Element IRBFE-N1: At $\eta = \eta_b$, this element uses information on $\partial\phi/\partial\eta$ and $\partial^2\phi/\partial\eta^2$. The resultant conversion system is

$$\begin{pmatrix} \frac{\partial\phi_b}{\partial\eta} \\ \phi_g \\ \frac{\partial^2\phi_b}{\partial\eta^2} \\ \frac{\partial\phi_g}{\partial\eta} \end{pmatrix} = \begin{pmatrix} I_b^{(1)}(\eta_b) & I_g^{(1)}(\eta_b) & 1 & 0 \\ I_b^{(0)}(\eta_g) & I_g^{(0)}(\eta_g) & \eta_g & 1 \\ I_b^{(2)}(\eta_b) & I_g^{(2)}(\eta_b) & 0 & 0 \\ I_b^{(1)}(\eta_g) & I_g^{(1)}(\eta_g) & 1 & 0 \end{pmatrix} \begin{pmatrix} w_b \\ w_g \\ C_1 \\ C_2 \end{pmatrix}, \tag{20}$$

Element IRBFE-N2: At $\eta = \eta_b$, this element uses information on ϕ and $\partial\phi/\partial\eta$. The corresponding conversion system is exactly the same as that of *IRBFE-D3*.

It should be pointed out that all nodal values at $\eta = \eta_b$ in *IRBFE-D1* and *IRBFE-D2* are given, while there is one nodal unknown at $\eta = \eta_b$ in *IRBFE-D3*, *IRBFE-N1* and *IRBFE-N2*. For the latter cases, one extra equation is needed and how to generate this equation will be discussed later. Tab. 1 provides a list of semi-interior elements and their characteristics. Owing to the facts that point collocation is used and the RBF conversion matrix is not over-determined, all boundary values here are imposed in an exact manner.

3.3 Incorporation of IRBFEs into the control-volume formulation

Assuming that a Cartesian-grid represents the problem domain Ω. In a control-volume approach, the domain is subdivided into a set of control volumes in such a way that there is one control volume surrounding each grid point without gaps

Table 1: List of semi-interior elements and their characteristics.

Boundary condition	Element	Nodal values at a boundary point	Unknowns
Dirichlet	*IRBFE-D1*	ϕ_b	None
	IRBFE-D2	ϕ_b and $\partial^2\phi_b/\partial\eta^2$	None
	IRBFE-D3	ϕ_b and $\partial\phi_b/\partial\eta$	$\partial\phi_b/\partial\eta$
Neumann	*IRBFE-N1*	$\partial\phi_b/\partial\eta$ and $\partial^2\phi_b/\partial\eta^2$	$\partial^2\phi_b/\partial\eta^2$
	IRBFE-N2	ϕ_b and $\partial\phi_b/\partial\eta$	ϕ_b

or overlapped volumes between adjacent elements. A typical control volume associated with a grid point P, denoted by Ω_P, is shown in Fig. 2, where E, W, N and S are the neighbouring points of P on the horizontal and vertical grid lines. The governing equation (8) is discretised by means of subregion collocation and this process is conducted in a similar fashion for all interior grid points of the problem domain.

By directly integrating (8) over Ω_P, the subregion-collocation equation is obtained

$$\int_{\Omega_P}\left(\frac{\partial^2\phi}{\partial x^2}+\frac{\partial^2\phi}{\partial y^2}-b(x,y)\right)d\Omega_P=0. \tag{21}$$

Applying the Gauss divergence theorem to (21) results in

$$\int_{\Gamma_P}\left(\frac{\partial\phi}{\partial x}dy-\frac{\partial\phi}{\partial y}dx\right)-\int_{\Omega_P}b(x,y)d\Omega_P=0, \tag{22}$$

where Γ_P denotes the faces of Ω_P. It is noted that partial derivatives of ϕ in (22) are of first order only and no approximation is made at this stage. Following the work of Patankar (1980), (22) reduces to

$$\left[\left(\frac{\partial\phi}{\partial x}\right)_e-\left(\frac{\partial\phi}{\partial x}\right)_w\right]\Delta y+\left[\left(\frac{\partial\phi}{\partial y}\right)_n-\left(\frac{\partial\phi}{\partial y}\right)_s\right]\Delta x-b(x_P,y_P)A_P=0, \tag{23}$$

where A_P is the area of Ω_P and the subscripts e, w, n and s are used to indicate that the flux is estimated at the intersections of the grid lines with the east, west, north and south faces of the control volume, respectively (Fig. 2).

In the presently proposed technique, 2-node IRBFEs, which are defined over line segments between P and its neighbouring grid points (E, W, N and S), are incorporated into (23) to represent the field variable ϕ and its derivatives. There are 4

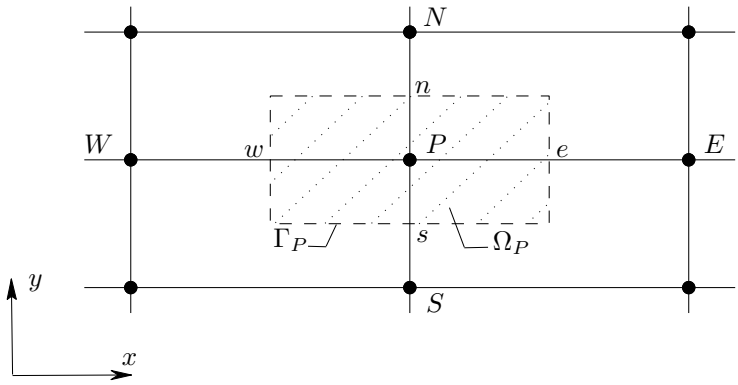

Figure 2: Schematic outline for a control volume in 2D.

IRBFEs associated with a control volume. Assuming that *PE* and *WP* are interior elements and making use of (15), the values of the flux at the faces $x = x_e$ and $x = x_w$ are computed as

$$\left(\frac{\partial \phi}{\partial x}\right)_e = \left[I_1^{(1)}(x_e), I_2^{(1)}(x_e), 1, 0\right] \mathscr{I}^{-1} \widehat{\psi} = \left[I_1^{(1)}(x_e), I_2^{(1)}(x_e), 1, 0\right] \mathscr{I}^{-1} \begin{pmatrix} \phi_P \\ \phi_E \\ \frac{\partial \phi_P}{\partial x} \\ \frac{\partial \phi_E}{\partial x} \end{pmatrix}$$

$$\text{with} \quad \eta_1 \equiv x_P \quad \text{and} \quad \eta_2 \equiv x_E, \tag{24}$$

$$\left(\frac{\partial \phi}{\partial x}\right)_w = \left[I_1^{(1)}(x_w), I_2^{(1)}(x_w), 1, 0\right] \mathscr{I}^{-1} \widehat{\psi} = \left[I_1^{(1)}(x_w), I_2^{(1)}(x_w), 1, 0\right] \mathscr{I}^{-1} \begin{pmatrix} \phi_W \\ \phi_P \\ \frac{\partial \phi_W}{\partial x} \\ \frac{\partial \phi_P}{\partial x} \end{pmatrix}$$

$$\text{with} \quad \eta_1 \equiv x_W \quad \text{and} \quad \eta_2 \equiv x_P, \tag{25}$$

where $I_1^{(1)}(x)$, $I_2^{(1)}(x)$ and $\mathscr{I}^{-1}$ are defined in (9)-(13). Vector $\widehat{\psi}$ may change if *PE* and *WP* are semi-interior elements. For example, one has

$$
\begin{aligned}
\widehat{\psi} &= (\phi_W, \phi_P, \partial\phi_P/\partial x)^T && \text{if } WP \text{ is a } D1 \text{ element,}\\
\widehat{\psi} &= \left(\phi_W, \partial^2\phi_W/\partial x^2, \phi_P, \partial\phi_P/\partial x\right)^T && \text{if } WP \text{ is a } D2 \text{ element,}\\
\widehat{\psi} &= (\phi_W, \partial\phi_W/\partial x, \phi_P, \partial\phi_P/\partial x)^T && \text{if } WP \text{ is a } D3 \text{ element,}\\
\widehat{\psi} &= \left(\partial\phi_W/\partial x, \partial^2\phi_W/\partial x^2, \phi_P, \partial\phi_P/\partial x\right)^T && \text{if } WP \text{ is a } N1 \text{ element,}\\
\widehat{\psi} &= (\phi_W, \partial\phi_W/\partial x, \phi_P, \partial\phi_P/\partial x)^T && \text{if } WP \text{ is a } N2 \text{ element.}
\end{aligned}
$$

Expressions for the flux at the faces $y = y_n$ and $y = y_s$ are of similar forms.

3.4 Inter-element C^2 continuity

It can be seen from IRBFE expressions for computing the flux at the faces (e.g. (24) and (25)), there are three unknowns, namely ϕ, $\partial\phi/\partial x$ and $\partial\phi/\partial y$, at a grid node P. Unlike conventional CVMs, the nodal values of $\partial\phi/\partial x$ and $\partial\phi/\partial y$ at P here constitute part of the nodal unknown vector. One thus needs to generate three independent equations. The first equation is obtained by conducting subregion-collocation of (8) at P, i.e. (23). The other two equations can be formed by enforcing the local continuity of $\partial^2\phi/\partial x^2$ and $\partial^2\phi/\partial y^2$ across the elements at P

$$\left(\frac{\partial^2\phi_P}{\partial x^2}\right)_L = \left(\frac{\partial^2\phi_P}{\partial x^2}\right)_R, \tag{26}$$

$$\left(\frac{\partial^2\phi_P}{\partial y^2}\right)_B = \left(\frac{\partial^2\phi_P}{\partial y^2}\right)_T, \tag{27}$$

where $(.)_L$ indicates that the computation of $(.)$ is based on the element to the left of P, i.e. element WP, and similarly subscripts R,B,T denote the right *(PE)*, bottom *(SP)* and top *(PN)* elements.

Substitution of (16) into (26) and (27) yields

$$\left(\left[I_1^{(2)}(\eta_2), I_2^{(2)}(\eta_2), 0, 0\right]\mathscr{I}^{-1}\widehat{\psi}\right)_L = \left(\left[I_1^{(2)}(\eta_1), I_2^{(2)}(\eta_1), 0, 0\right]\mathscr{I}^{-1}\widehat{\psi}\right)_R, \tag{28}$$

where η represents x and $\eta_2 \equiv \eta_1 \equiv x_P$, and

$$\left(\left[I_1^{(2)}(\eta_2), I_2^{(2)}(\eta_2), 0, 0\right]\mathscr{I}^{-1}\widehat{\psi}\right)_B = \left(\left[I_1^{(2)}(\eta_1), I_2^{(2)}(\eta_1), 0, 0\right]\mathscr{I}^{-1}\widehat{\psi}\right)_T, \tag{29}$$

where η represents y and $\eta_2 \equiv \eta_1 \equiv y_P$. The conditions (26)-(27) or (28)-(29) guarantee that the solution ϕ across IRBFEs is a C^2 function.

As discussed earlier, for *IRBFE-D3*, *IRBFE-N1* and *IRBFE-N2* elements, there is one unknown at a boundary node and one more extra equation needs be formed. This equation can be generated by integrating (8) over a half control-volume associated with that boundary node (Patankar (1980)).

Collection of the discretised equations at the appropriate nodal points and the continuity equations at the interior grid points leads to a square system of algebraic equations that is sparse and banded. Two-point line elements are well suited to discretisation methods based on Cartesian grids.

4 Numerical results

IRBFEs are now validated through function approximation and solution of boundary-value problems governed by ODEs and PDEs. For all numerical examples presented in this study, the MQ width a is simply chosen proportionally to the element length h by a factor β. The value of β is considered in a wide range from 1 to 85 to study its influence on the accuracy. In the case of non-rectangular domains, there may be some nodes that are too close to the boundary. If an interior node falls within a distance of $h/2$ to the boundary, such a node is removed from the set of nodal points.

The solution accuracy of an approximation scheme is measured by means of the discrete relative L_2 errors for the field variable and its first-order partial derivatives

$$N_e(\phi) = \frac{\sqrt{\sum_{i=1}^{M}\left(\phi_i^{(e)} - \phi_i\right)^2}}{\sqrt{\sum_{i=1}^{M}\left(\phi_i^{(e)}\right)^2}}, \tag{30}$$

$$N_e\left(\frac{\partial \phi}{\partial x}\right) = \frac{\sqrt{\sum_{i=1}^{M}\left(\frac{\partial \phi_i^{(e)}}{\partial x} - \frac{\partial \phi_i}{\partial x}\right)^2}}{\sqrt{\sum_{i=1}^{M}\left(\frac{\partial \phi_i^{(e)}}{\partial x}\right)^2}}, \tag{31}$$

$$N_e\left(\frac{\partial \phi}{\partial y}\right) = \frac{\sqrt{\sum_{i=1}^{M}\left(\frac{\partial \phi_i^{(e)}}{\partial y} - \frac{\partial \phi_i}{\partial y}\right)^2}}{\sqrt{\sum_{i=1}^{M}\left(\frac{\partial \phi_i^{(e)}}{\partial y}\right)^2}}, \tag{32}$$

where the superscript (e) refers to the exact solution and M is the length of a test set that is comprised of groups of 500 uniformly distributed points on grid lines. Another important measure is the convergence rate of the solution with respect to the refinement of spatial discretisation

$$N_e(h) \approx \gamma h^{\alpha} = O(h^{\alpha}), \tag{33}$$

in which α and γ are exponential model's parameters. Given a set of observations, these parameters can be found by the general linear least squares technique. To assess the performance of the proposed technique, the standard CVM (Patankar (1980)) is also implemented here.

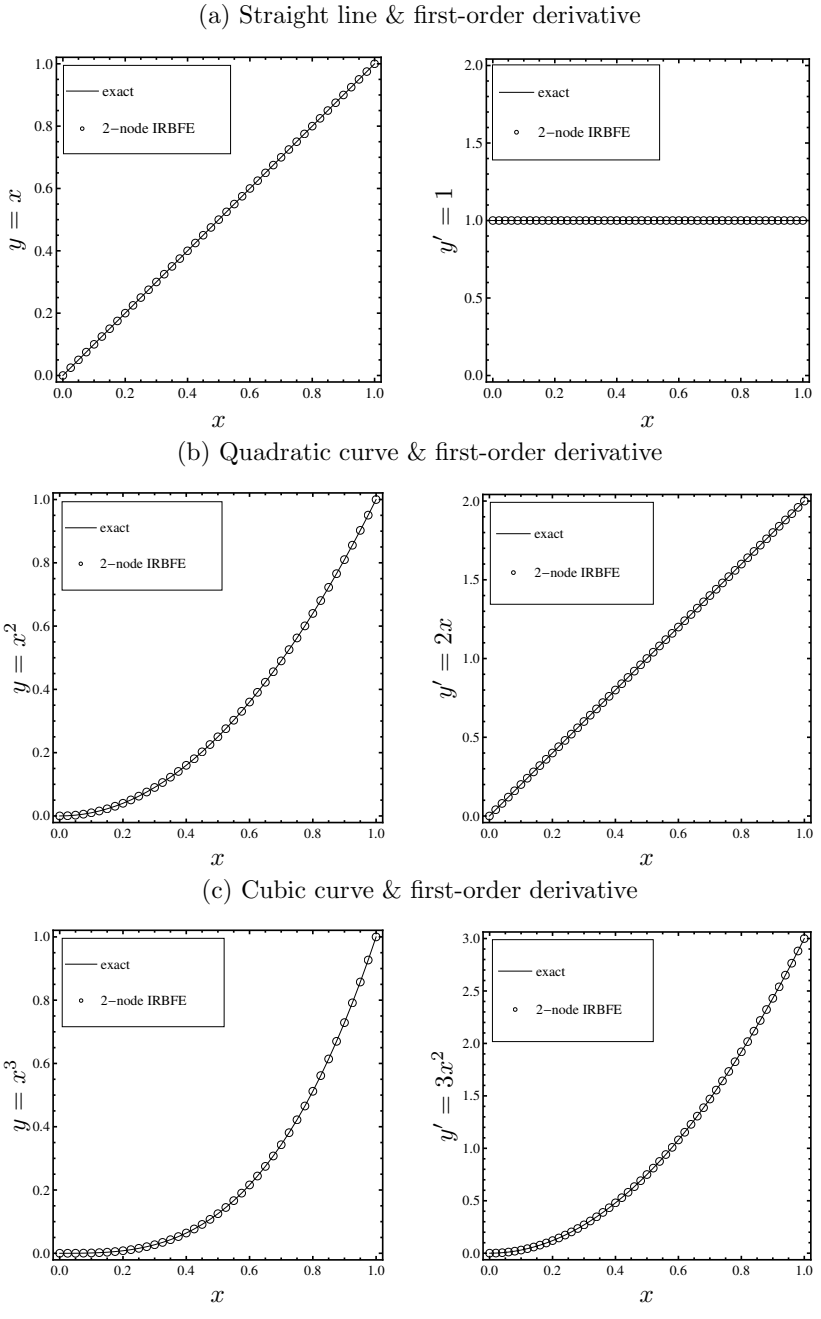

Figure 3: Function approximation: Approximation for functions (left) and their first-order derivative (right) by using one IRBFE only. It can be seen that the present two-node IRBFE is able to produce non-linear behaviours (i.e. curved lines) between the two extremes.

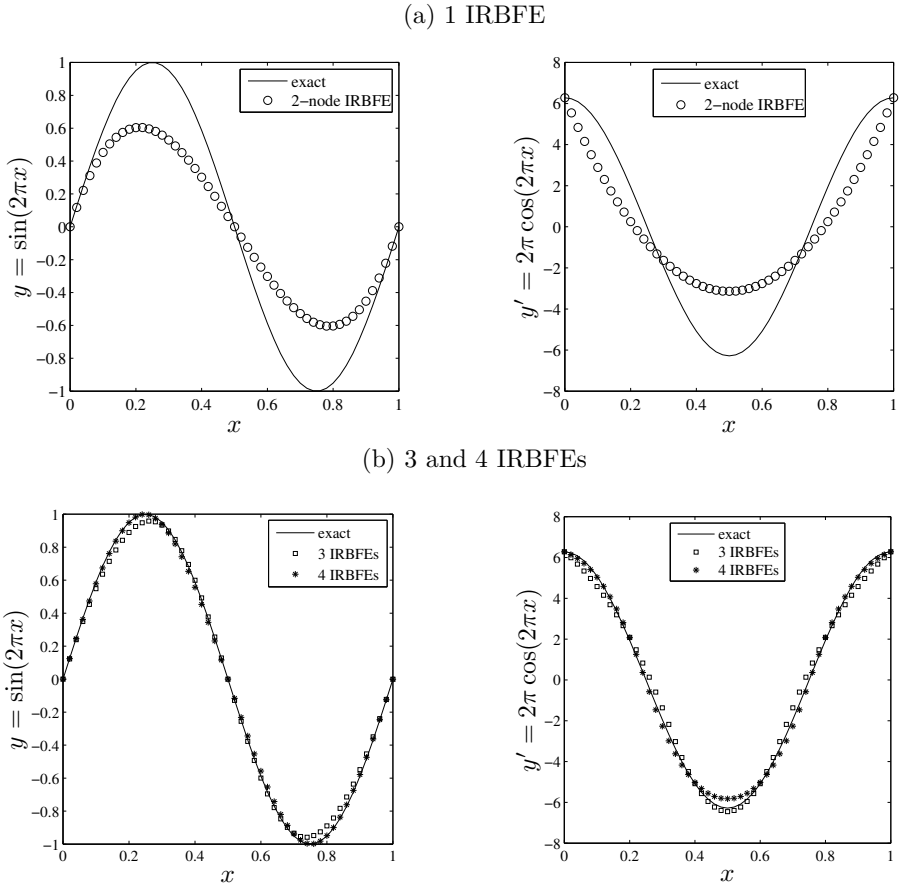

Figure 4: Function approximation (*continued*), trigonometric function: Approximations for the function (left) and its first-order derivative (right).

4.1 Function approximation

The present 2-node IRBFE scheme is first applied to the representation of functions. Consider four different test functions, namely straight line $y = x$, quadratic curve $y = x^2$, cubic curve $y = x^3$ and trigonometric function $y = \sin(2\pi x)$. The domain of interest is $[0,1]$ that is represented by one element only. Values of y and dy/dx are given at $x = 0$ and $x = 1$. Fig. 3 shows the plots of the approximate and exact functions for the first three cases where good agreement is achieved with only one element. It should be pointed out that, for the second and third functions, curved lines are reproduced even only two nodes (i.e. only one element) are em-

ployed. The fourth function $y = \sin(2\pi x)$ is infinitely smooth and it is clear that one can construct several other approximate functions that would satisfy the four given input data. The present scheme picks up one of them, probably the simplest one (Fig. 4a). As more elements are used, a closer approximation to the exact function is obtained as shown in Fig. 4b. Numerical results for the last three functions show that the present two-node IRBFE has the ability to produce curved lines between its two extremes. This can be seen as a strength of IRBFEs over linear elements used in conventional techniques.

4.2 Solution of ODEs

4.2.1 Problem 1

Consider a 1D problem governed by

$$\frac{d}{dx}\left(\frac{d\phi}{dx}\right) + \phi + x = 0, \qquad 0 \le x \le 1, \tag{34}$$

and subject to two cases of boundary conditions

Case 1: $\phi(0) = 0$ and $\phi(1) = 0$ (Dirichlet boundary conditions only)
Case 2: $\phi(0) = 0$ and $d\phi(1)/dx = \cot(1) - 1$ (Dirichlet and Neumann boundary conditions).

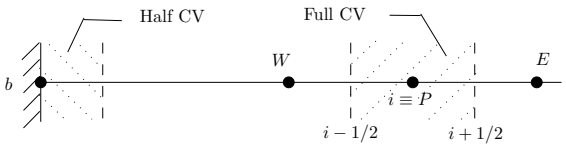

Figure 5: Control volumes associated with interior and boundary nodes in 1D.

The exact solution of this problem can be verified to be

$$\phi^{(e)}(x) = \frac{\sin(x)}{\sin(1)} - x. \tag{35}$$

The problem domain is discretised by n uniformly-distributed points. Each node x_i is associated with a control volume denoted by Ω_i. For $2 \le i \le n-1$, Ω_i is defined

(a) Field variable

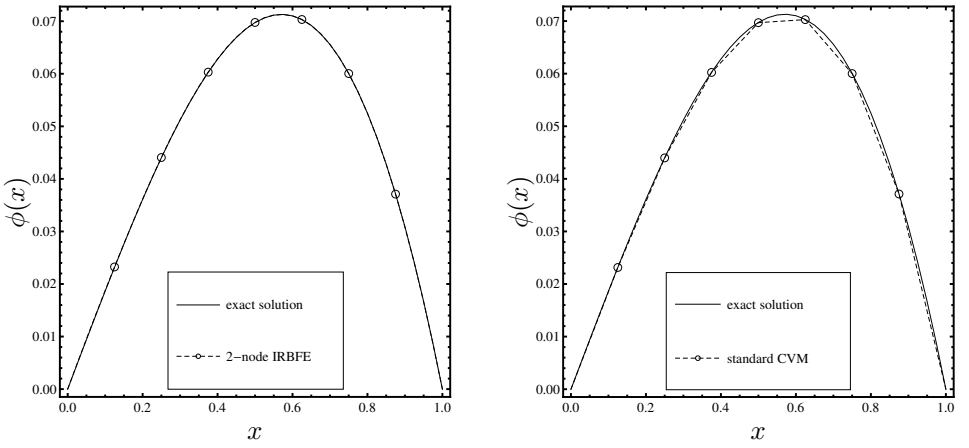

(b) First-order derivative

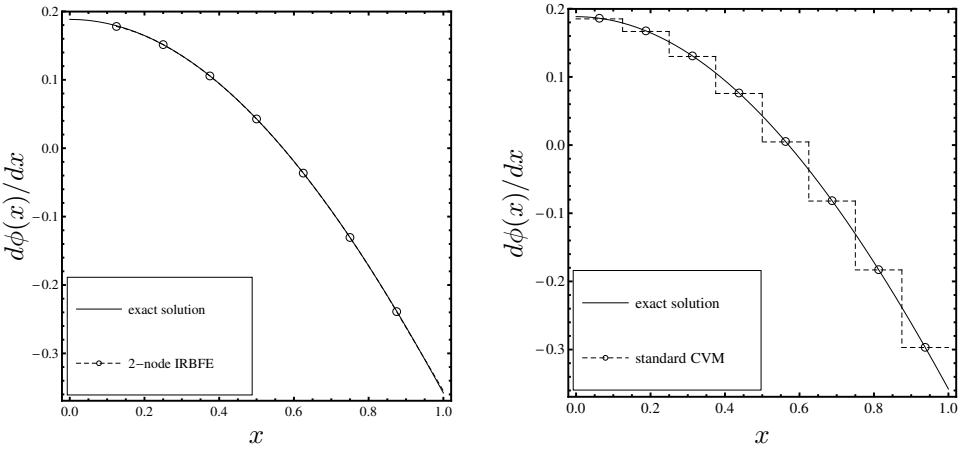

Figure 6: ODE, Problem 1, Dirichlet boundary conditions, $n = 9$: Comparison of the exact and approximate solutions for ϕ and $d\phi/dx$ by the present *D1-D1* strategy (left) and the standard CV method (right).

as $[x_{i-1/2}, x_{i+1/2}]$ (full CV). For $i = 1$ and $i = n$, Ω_i is taken to be $[x_1, x_{1+1/2}]$ and $[x_{n-1/2}, x_n]$ (half CV), respectively. A schematic outline of a full CV and a half CV is presented in Fig. 5. Generally speaking, to form a set of algebraic equations, (34) is integrated over full CVs at x_i with $i = (2, 3, \cdots, n-1)$ for Case 1, and over full CVs at x_i with $i = (2, 3, \cdots, n-1)$ and a half CV at x_n for Case 2. The resultant system is thus of dimensions $(n-2) \times (n-2)$ for Case 1 and $(n-1) \times (n-1)$ for Case 2.

Hereafter, *Di-Dj* is used to denote the boundary treatment strategy in which the boundary region $[x_1, x_2]$ is represented by element *IRBFE-Di* and $[x_{n-1}, x_n]$ by *IRBFE-Dj*, while *Di-Nj* represents the strategy in which $[x_1, x_2]$ and $[x_{n-1}, x_n]$ are modelled by elements *IRBFE-Di* and *IRBFE-Nj*, respectively. We employ the values of n ranging from 7 to 151 for h-adaptivity studies and the values of β from 1 to 85 for β-adaptivity studies.

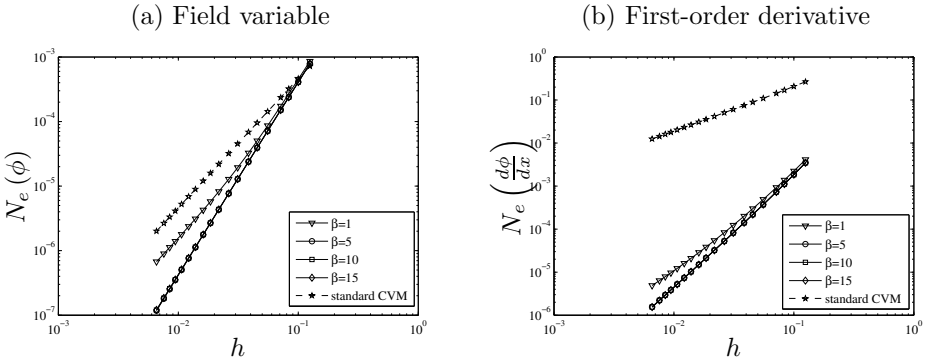

Figure 7: ODE, Problem 1, Dirichlet boundary conditions: h-adaptivity studies conducted with several values of β for the *D1-D1* strategy. It is noted that results with $\beta = (5, 10, 15)$ are undistinguishable.

Case 1: Fig. 6 shows the plots of ϕ and $d\phi/dx$ by the proposed technique using the *D1-D1* strategy and by the standard CVM. It can be seen that the present solution is smooth for both ϕ and $d\phi/dx$ even with only a few interior nodes used. On the other hand, using linear interpolations, the standard CV solution for $d\phi/dx$ has a stair-case shape. To alleviate this zigzag variation, much more grid points are needed. Grid convergence studies for the proposed method employed with various values of β and for the standard CVM are depicted in Fig. 7. It can be seen that the former outperforms the latter. At dense grids, in terms of the error N_e, the results for $d\phi/dx$ show a remarkable four orders of magnitude improvement (Fig. 7b).

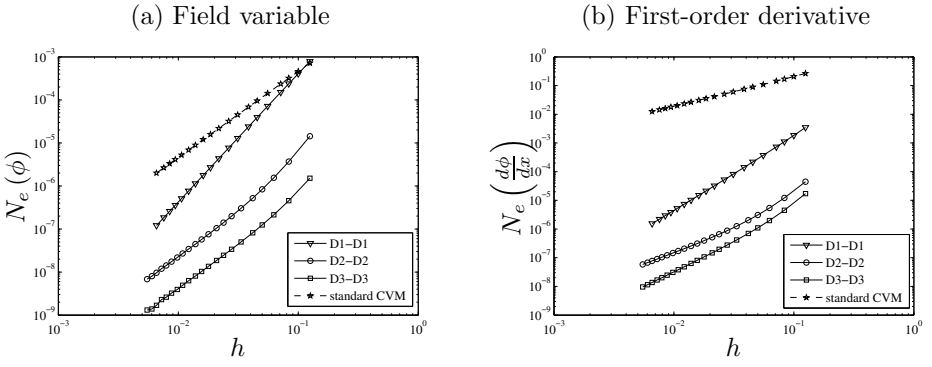

Figure 8: ODE, Problem 1, Dirichlet boundary conditions: Effects of types of semi-interior elements on the solution accuracy for $\beta = 15$.

Fig. 8 and Tab. 2 compare the performance of the proposed method among three types of semi-interior element strategies, namely *D1-D1*, *D2-D2* and *D3-D3*. Results obtained by the standard CVM are also included and they are taken here as the reference. With more information incorporated into the IRBFE approximations, the *D2-D2* and *D3-D3* strategies yield much more accurate results than *D1-D1*, and *D3-D3* works better than *D2-D2* as shown in Fig. 8a-b. Tab. 2 indicates that rates obtained by the three strategies are generally higher than those by the standard CVM. For example, *D1-D1* yields $O(h^{2.99})$ for ϕ and $O(h^{2.61})$ for $d\phi/dx$, while the standard CVM gives $O(h^{2.00})$ for ϕ and $O(h^{1.03})$ for $d\phi/dx$. An improvement in the approximation quality for $d\phi/dx$ is thus much bigger than that for ϕ. It should be noted that *D1-D1* exhibits higher rates of grid convergence but produces less accurate results than *D2-D2* and *D3-D3*.

In Fig. 9, the effects of β on the solution accuracy for coarse ($n = 9$) and dense ($n = 153$) grids are studied. As β increases, the overall error of the IRBFE solution is first reduced and then becomes flat/fluctuated. There are dramatic reductions (i.e. exponential convergence) in $N_e(\phi)$ and $N_e(d\phi/dx)$ for the *D2-D2* and *D3-D3* strategies. In the case of large n and using *D2-D2* and *D3-D3*, it appears that there exists an optimal value for β, e.g. $\beta = 42$ for *D2-D2* and $\beta = 32$ for *D3-D3*. Nevertheless, the present method can work with a wide range of β. This ability is also clearly seen in Fig. 7.

Case 2: Results obtained by the *D1-N1* and *D1-N2* strategies using $\beta = 1$ and $\beta = 15$ and by the standard CVM are depicted in Fig. 10. The two strategies have similar performances which are far superior to that by the standard CVM. At

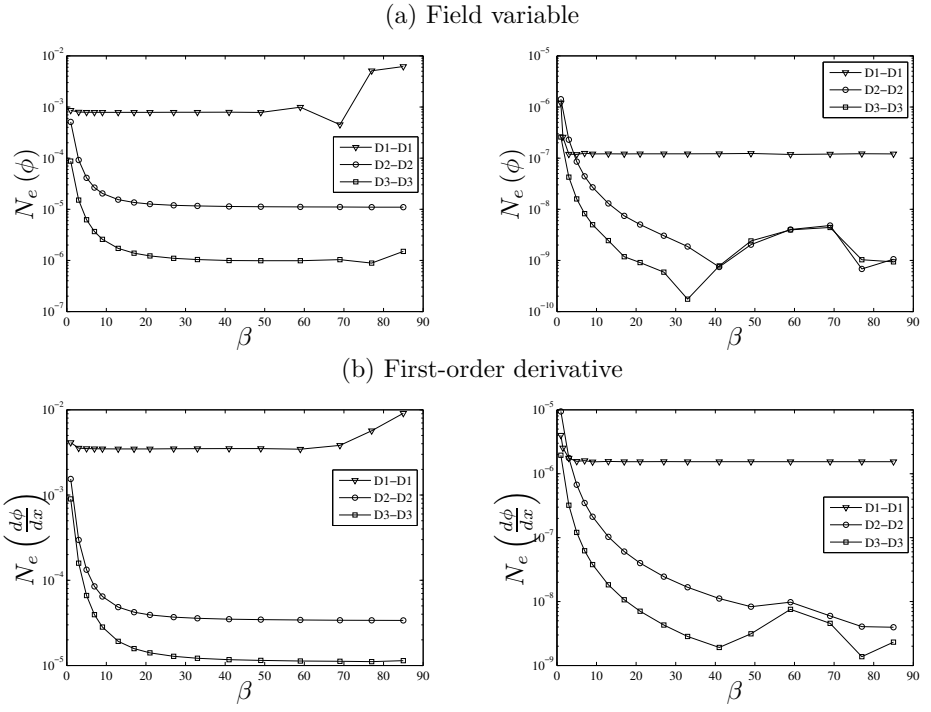

Figure 9: ODE, Problem 1, Dirichlet boundary conditions: β-adaptivity studies conducted with $n = 9$ (left) and $n = 153$ (right) for three boundary treatment strategies.

dense grids, an improvement is up to one order of magnitude for ϕ and four orders of magnitude for $d\phi/dx$. It is also observed that β can be used as an effective tool to enhance the solution accuracy. Tab. 3 shows that the present two schemes converge faster than the standard CVM. For example, the rates are $O(h^{3.02})$ for ϕ and $O(h^{2.53})$ for $d\phi/dx$ by the present two strategies ($\beta = 15$), and $O(h^{1.97})$ for ϕ and $O(h^{1.03})$ for $d\phi/dx$ by the standard CVM.

4.2.2 Problem 2

In this example, the ODE involves more terms and its solution is highly oscillatory. The equation takes the form

$$\frac{d^2\phi}{dx^2} + \frac{d\phi}{dx} + \phi = -e^{-5x}\left(9979\sin(100x) + 900\cos(100x)\right), \qquad 0 \le x \le 1. \quad (36)$$

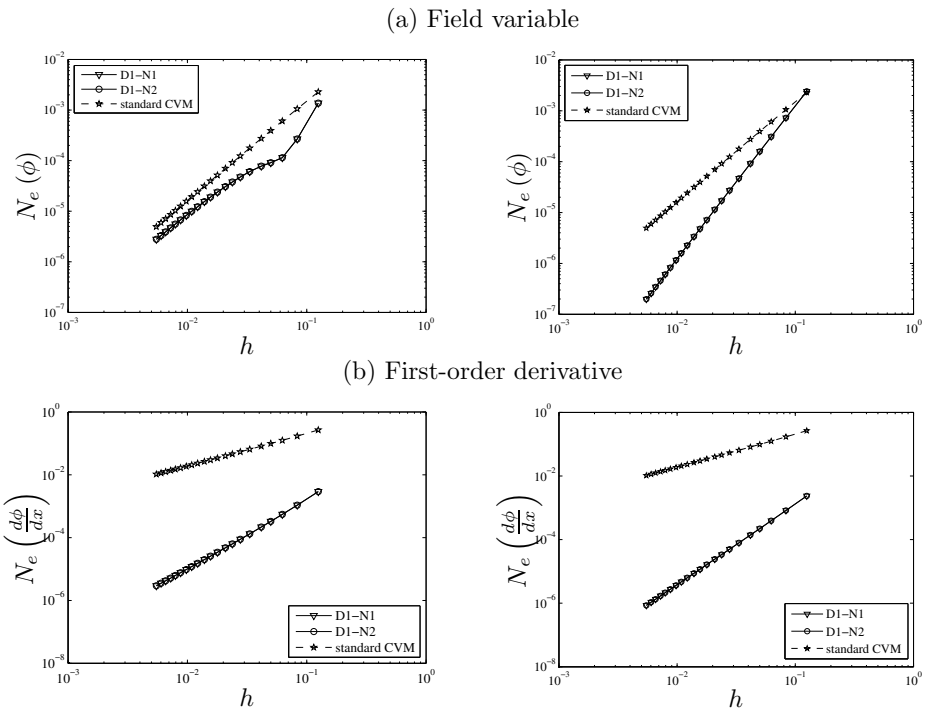

Figure 10: ODE, Problem 1, Dirichlet and Neumann boundary conditions: Effects of types of semi-interior elements on the solution accuracy for $\beta = 1$ (left) and $\beta = 15$ (right). It is noted that plots have the same scaling and results by the two boundary treatment strategies are undistinguishable.

We consider two cases of boundary conditions: Dirichlet-Dirichlet (Case 1) and Dirichlet-Neumann (Case 2). The plots of the exact solution $\phi^{(e)} = \sin(100x)e^{-5x}$ and its first-order derivative are shown in Fig. 11. Computations are conducted with the values of n varying from 23 to 403 and the values of β from 1 to 80. Results concerning h adaptivity and β adaptivity are presented in Fig. 12, Fig. 13 and Tab. 4 for Case 1, and in Fig. 14 and Tab. 5 for Case 2. Remarks here are similar to those in Problem 1. It should be pointed out that

(i) very high rates of grid convergence, i.e. up to $O(h^{4.23})$ for ϕ and $O(h^{3.80})$ for $d\phi/dx$ (Case 1), and $O(h^{4.38})$ for ϕ and $O(h^{3.92})$ for $d\phi/dx$ (Case 2), are achieved here,

(ii) the IRBFE solution is very stable (i.e. no fluctuation) at large values of β,

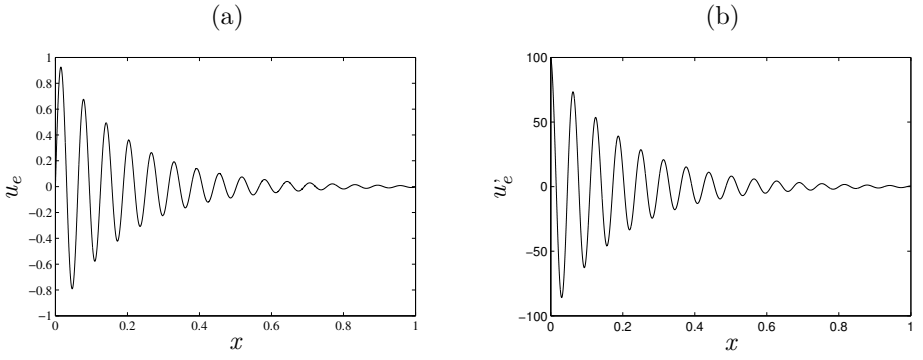

Figure 11: ODE, Problem 2: Exact solution (a) and its first-order derivative (b).

(iii) given a grid size h and a value of β, the overall errors for Case 2 are as low as those for Case 1,

(iv) the accuracy improvement is more significant for $d\phi/dx$ than for ϕ.

This problem (Case 1) was also solved in Mai-Duy and Tran-Cong (2008) using the multidomain (MD) RBF collocation method. Two versions, namely differentiated-RBF (MD-DRBF) and integrated-RBF (MD-IRBF) schemes, were implemented. Using two non-overlapping subdomains, $\beta = 1$ and 201 nodes/subdomain (i.e. 401 nodes for the whole domain), the obtained N_e errors for ϕ were 0.2 for MD-DRBF and 2.72×10^{-4} for MD-IRBF. Using the same set of nodes (i.e. 401 points or 400 IRBFEs), $\beta = 15$ and *D3-D3*, the present method yields $N_e = 1.28 \times 10^{-5}$, which is much lower than those by the MD-RBF collocation method. It is noted that conventional/global RBF methods are able to work with low values of β such as $\beta = 1$.

4.3 Solution of PDEs

The proposed CV method is further validated through the solution of PDEs on both rectangular and non-rectangular domains. Elements *IRBFE-D1* and *IRBFE-D2* are employed to deal with Dirichlet boundary conditions, while *IRBFE-N2* is used for Neumann boundary conditions. It is noted that *IRBFE-D1* can be applicable to problems with regular as well as irregular geometries. All IRBFE calculations here are carried out with two values of β, namely 1 and 15.

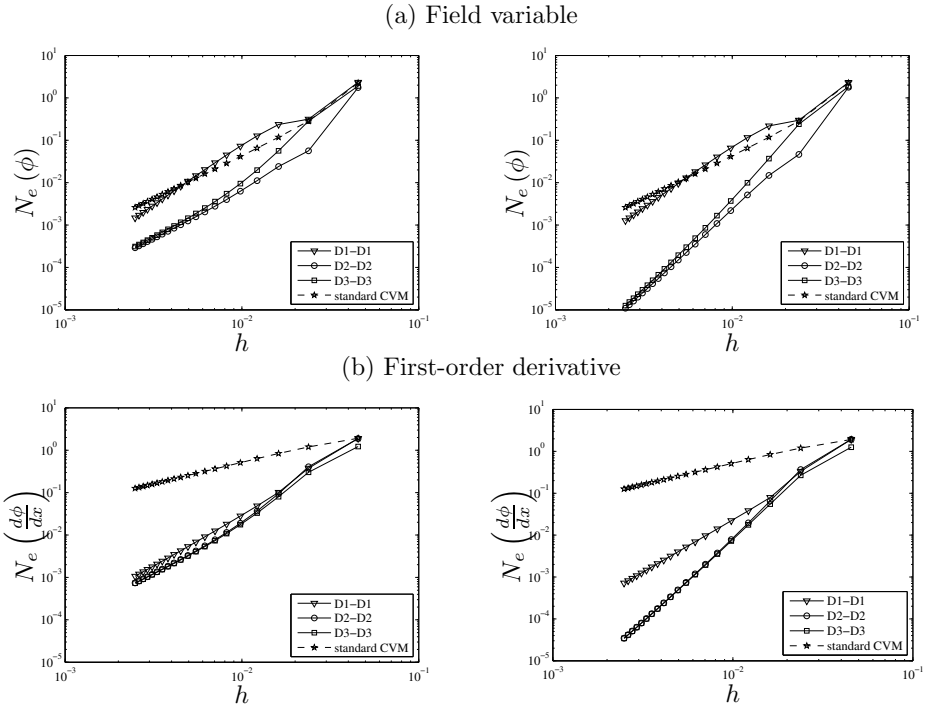

Figure 12: ODE, Problem 2, Dirichlet boundary conditions: h-adaptivity studies conducted with $\beta = 1$ (left) and $\beta = 15$ (right).

4.3.1 Problem 1: rectangular domain

Consider the following Poisson equation

$$\frac{\partial^2 \phi}{\partial x^2} + \frac{\partial^2 \phi}{\partial y^2} = -2\pi^2 \cos(\pi x)\cos(\pi y), \tag{37}$$

on a square domain $0 \leq x, y \leq 1$ with two different cases of boundary conditions Case 1:

$$\begin{aligned}
&\phi = \cos(\pi y) \quad \text{for} \quad x = 0,\ 0 \leq y \leq 1 \\
&\phi = -\cos(\pi y) \quad \text{for} \quad x = 1,\ 0 \leq y \leq 1 \\
&\phi = \cos(\pi x) \quad \text{for} \quad y = 0,\ 0 \leq x \leq 1 \\
&\phi = -\cos(\pi x) \quad \text{for} \quad y = 1,\ 0 \leq x \leq 1
\end{aligned}$$

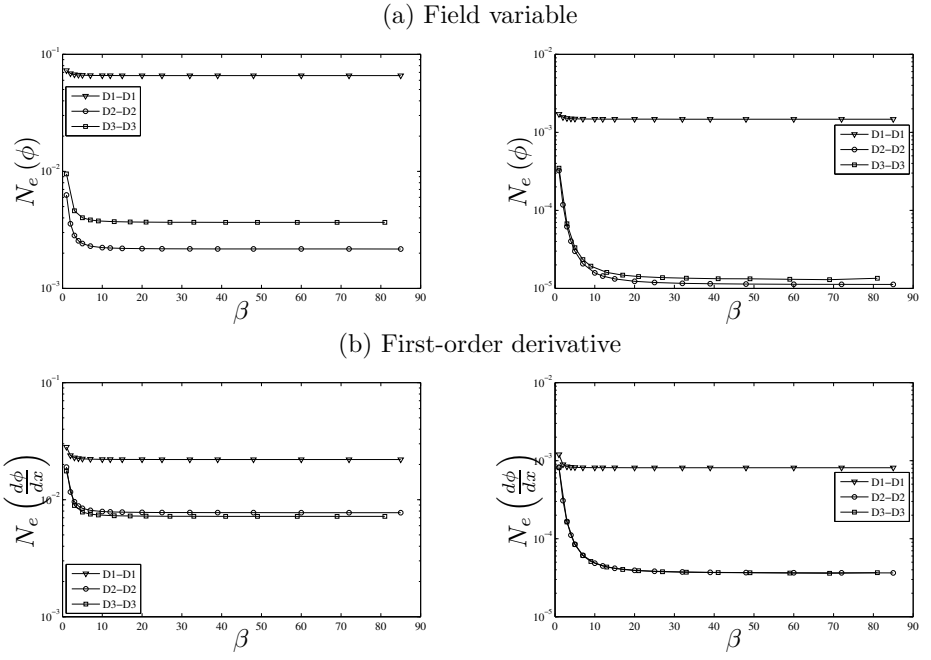

Figure 13: ODE, Problem 2: β-adaptivity studies conducted with $n = 103$ (left) and $n = 383$ (right) for three different semi-interior element strategies.

Case 2:

$$\begin{aligned}
\phi &= \cos(\pi y) && \text{for} && x = 0,\ 0 \le y \le 1 \\
\phi &= -\cos(\pi y) && \text{for} && x = 1,\ 0 \le y \le 1 \\
\frac{\partial \phi}{\partial y} &= 0 && \text{for} && y = 0,\ 0 \le x \le 1 \\
\frac{\partial \phi}{\partial y} &= 0 && \text{for} && y = 1,\ 0 \le x \le 1.
\end{aligned}$$

The exact solution to this problem can be verified to be

$$\phi^{(e)}(x,y) = \cos(\pi x)\cos(\pi y). \tag{38}$$

In Case 1 (i.e. Dirichlet boundary conditions only), the system of algebraic equations is generated by integrating (37) over full CVs associated with the interior nodes. In Case 2 (i.e. Dirichlet and Neumann boundary conditions), apart from the interior nodal variable values, there are additional unknown values of ϕ at the

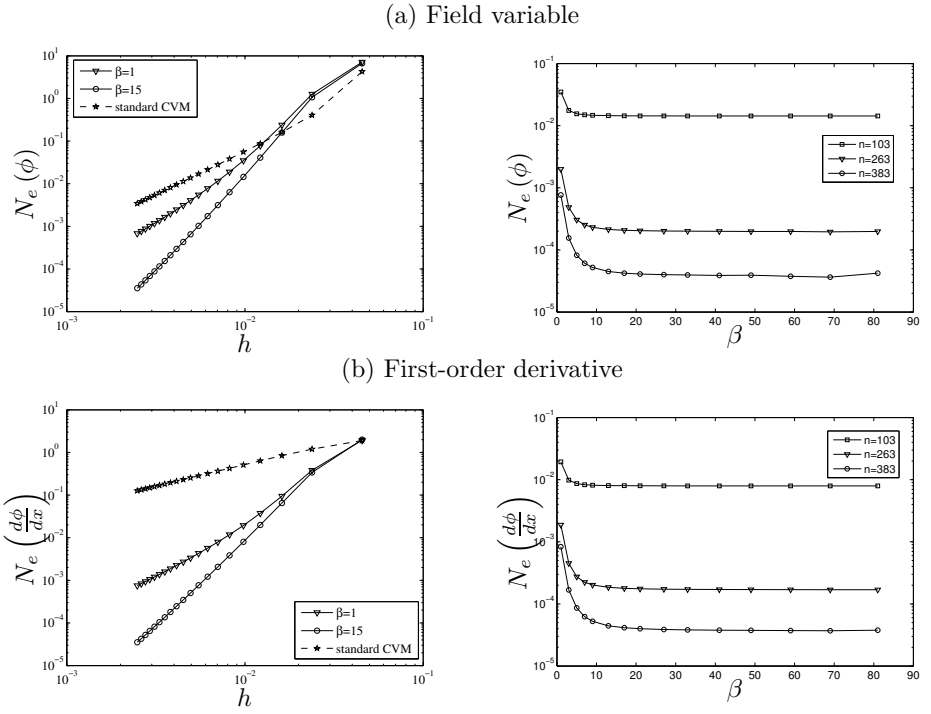

Figure 14: ODE, Problem 2, Dirichlet and Neumann boundary conditions: h-adaptivity (left) and β-adaptivity (right) studies for the *D3-N2* strategy.

boundary nodes on $y = 0$ and $y = 1$. As a result, one needs to generate not only full-CV equations associated with the interior nodes but also half-CV equations associated with the boundary nodes on $y = 0$ and $y = 1$. For the latter (Fig. 15), the IRBFE approximations on $y = 0$ and $y = 1$ are constructed as in the case of a grid line and hence the approximate solution ϕ is also C^2-continuous on these lines. It can be seen that the size of the discretised system in Case 2 is slightly larger than that in Case 1.

To study the convergent behaviour of the proposed technique, various grids, namely (5×5, 9×9,..., 73×73), are employed. Results concerning the relative L_2 error and the rate of convergence with grid refinement by the present and standard CV methods are shown in Fig. 16 for Case 1, Fig. 17 for Case 2, and Tab. 6 for Case 1 and Case 2.

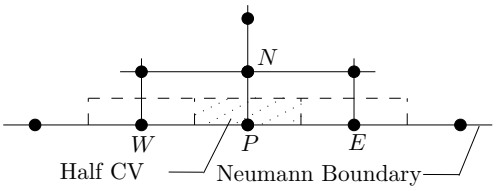

Figure 15: Half control volume associated with a boundary node in 2D.

Table 2: ODE, Problem 1, Dirichlet boundary conditions: rates of convergence $O(h^\alpha)$ for ϕ and $\partial\phi/\partial x$ for several large β values and semi-interior element types.

	α					
	ϕ			$\partial\phi/\partial x$		
β	*D1-D1*	*D2-D2*	*D3-D3*	*D1-D1*	*D2-D2*	*D3-D3*
5	2.995	2.057	2.009	2.604	1.719	2.096
10	2.987	2.188	2.086	2.606	1.842	2.180
15	2.985	2.332	2.185	2.606	1.983	2.283
20	2.984	2.475	2.332	2.606	2.119	2.391
Standard CVM		2.000			1.034	

Table 3: ODE, Problem 1, Dirichlet-Neumann boundary conditions: rates of convergence $O(h^\alpha)$ for ϕ and $\partial\phi/\partial x$ for two semi-interior element types.

	α			
	ϕ		$\partial\phi/\partial x$	
β	*D1-N1*	*D1-N2*	*D1-N1*	*D1-N2*
1	1.722	1.722	2.183	2.183
15	3.016	3.016	2.529	2.529
Standard CVM	1.971		1.029	

Table 4: ODE, Problem 2, Dirichlet boundary conditions: rates of convergence $O(h^{\alpha})$ for ϕ and $\partial\phi/\partial x$ for several β values and semi-interior element types.

	α			
	ϕ		$\partial\phi/\partial x$	
Boundary treatment	$\beta = 1$	$\beta = 15$	$\beta = 1$	$\beta = 15$
D1-D1	2.540	2.582	2.554	2.670
D2-D2	2.679	3.965	2.713	3.932
D3-D3	2.971	4.229	2.588	3.801
Standard CVM	2.194		0.971	

Table 5: ODE, Problem 2, Dirichlet and Neumann boundary conditions, *D3-N2* treatment: rates of convergence $O(h^{\alpha})$ for ϕ and $\partial\phi/\partial x$ for several β values.

	α	
β	ϕ	$\partial\phi/\partial x$
1	3.240	2.706
15	4.380	3.919
Standard CVM	2.268	0.970

Table 6: PDE, Problem 1 and Problem 2: Rates of grid convergence $O(h^{\alpha})$ for the field variable and its first-order partial derivatives, (1): standard CVM.

	α								
	Problem 1 (Rectangular domain)								Problem 2 (Circular domain)
	Dirichlet					Dirichlet & Neumann			Dirichlet
		D1-D1		*D2-D2*			*D1-N2*		*D1-D1*
	(1)	$\beta = 1$	$\beta = 15$	$\beta = 1$	$\beta = 15$	(1)	$\beta = 1$	$\beta = 15$	$\beta = 15$
ϕ	1.997	2.262	2.273	2.089	2.094	1.997	2.141	2.149	2.223
$\partial\phi/\partial x$	0.997	1.787	2.350	1.583	2.101	0.997	1.833	2.200	2.140
$\partial\phi/\partial y$	0.997	1.787	2.350	1.583	2.101	0.997	1.566	2.171	2.144

(a) Field variable

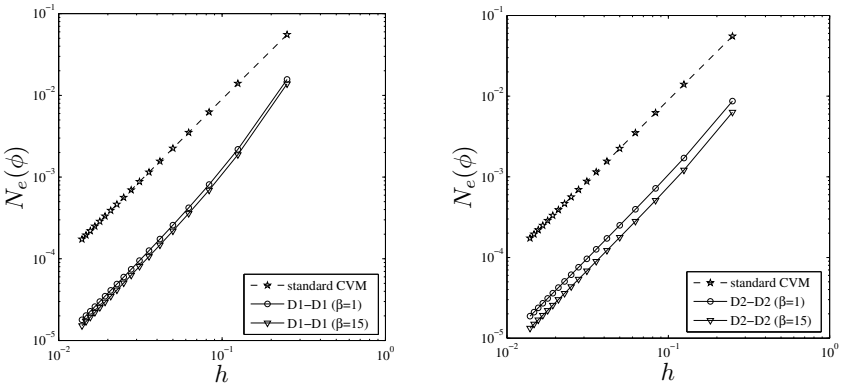

(b) First-order derivative with respect to x

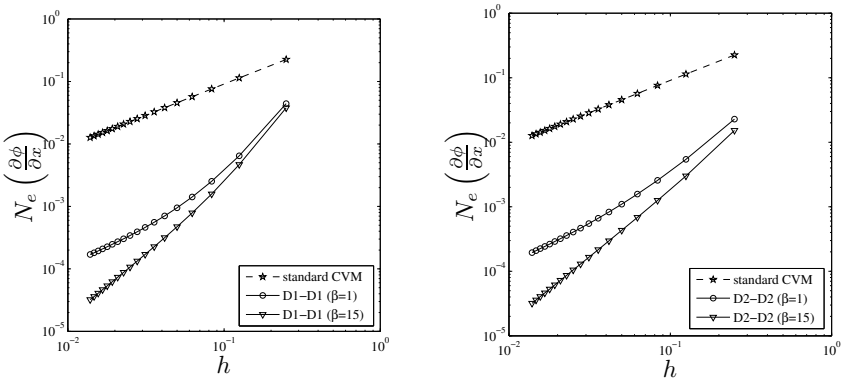

(c) First-order derivative with respect to y

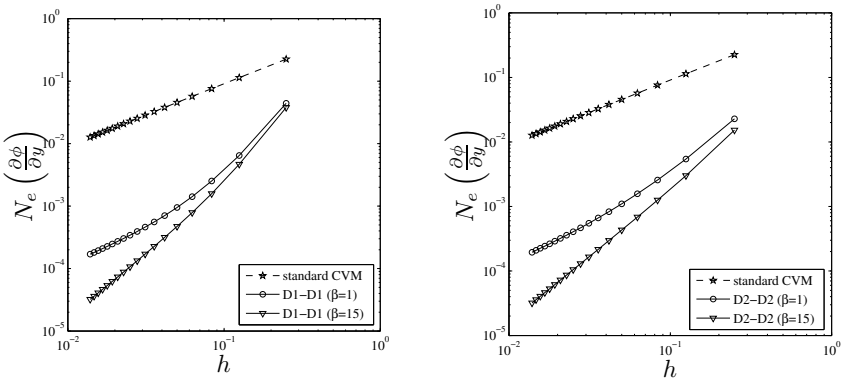

Figure 16: PDE, Problem 1, rectangular domain, Dirichlet boundary conditions: *h*-adaptivity studies for the *D1-D1* (left) and *D2-D2* (right) strategies.

It can be seen from Fig. 16 and Fig. 17, the present *D1-D1*, *D2-D2* and *D1-N2* strategies employed with a wide range of β produce much more accurate results especially for $\partial\phi/\partial x$ and $\partial\phi/\partial y$ than the standard CV method. For instance, at a grid of 73×73 and $\beta = 15$, the improvement is about one order of magnitude for the field variable and about three orders of of magnitude for its first-order partial derivatives. For Case 1 (Fig. 16), results at coarse grids by the *D2-D2* strategy are a bit more accurate than those by *D1-D1*, probably owing to the fact that the former uses information about (37) on the boundary.

It can be seen from Tab. 6, the present method yields a faster convergence, especially for $\partial\phi/\partial x$ and $\partial\phi/\partial y$, than the standard CV method for both Case 1 and Case 2. For example, in Case 1, the solutions $\partial\phi/\partial x$ and $\partial\phi/\partial y$ converge at the rate $O(h^{2.35})$ using the *D1-D1* strategy, $O(h^{2.10})$ using *D2-D2*, and $O(h^{1.00})$ using the standard CV method.

Like in 1D problems, the use of $\beta = 15$ (i.e. large values) here also leads to better accuracy and faster convergence especially for first-order partial derivatives than the use of $\beta = 1$ (i.e. small values), and the IRBFE solutions for Case 1 and Case 2 have similar degrees of accuracy.

4.3.2 Problem 2: circular domain

Find ϕ such that

$$\frac{\partial^2\phi}{\partial x^2}+\frac{\partial^2\phi}{\partial y^2}=0, \tag{39}$$

on a circular domain of radius $\pi/2$ centred at $(\pi/2,\pi/2)$ with Dirichlet boundary conditions. The exact solution to this problem is chosen to be

$$\phi^{(e)}(x,y)=\frac{1}{\sinh(\pi)}\sin(x)\sinh(y), \tag{40}$$

from which one can easily derive the boundary values of ϕ.

The problem domain is discretised by a Cartersian grid as shown in Fig. 18. Calculations are carried out with grids of (5×5, 11×11,..., 151×151) and $\beta = 15$. We employ semi-interior elements *IRBFE-D1* for the handling of boundary conditions. Results obtained are presented in Fig. 19, which plots the solution accuracy N_e against the grid size h. It can be seen that the error is consistently reduced as a grid is refined.

Tab. 6 also compares the rate of convergence by the proposed technique between Problem 1 (rectangular domain) and Problem 2 (circular domain). Using the same *D1-D1* strategy and $\beta = 15$, the orders of accuracy of the solutions ϕ, $\partial\phi/\partial x$ and

(a) Field variable

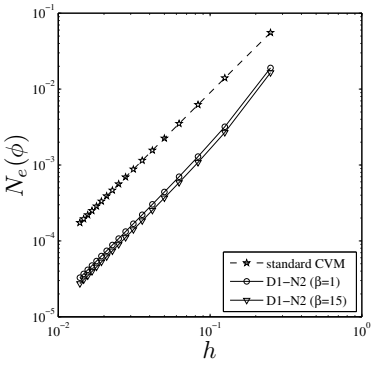

(b) First-order derivative with respect to x

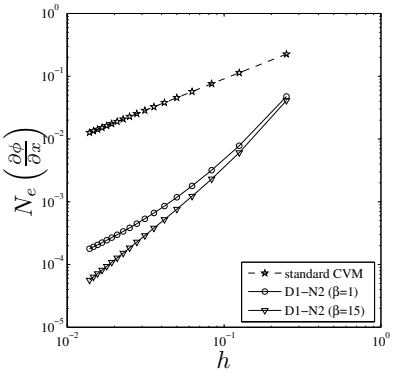

(c) First-order derivative with respect to y

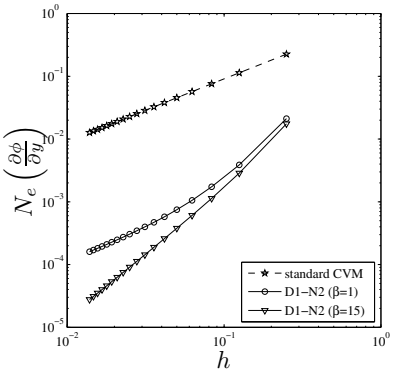

Figure 17: PDE, Problem 1, rectangular domain, Dirichlet and Neumann boundary conditions: h-adaptivity studies conducted with $\beta = 1$ and $\beta = 15$ for the *D1-N2* strategy.

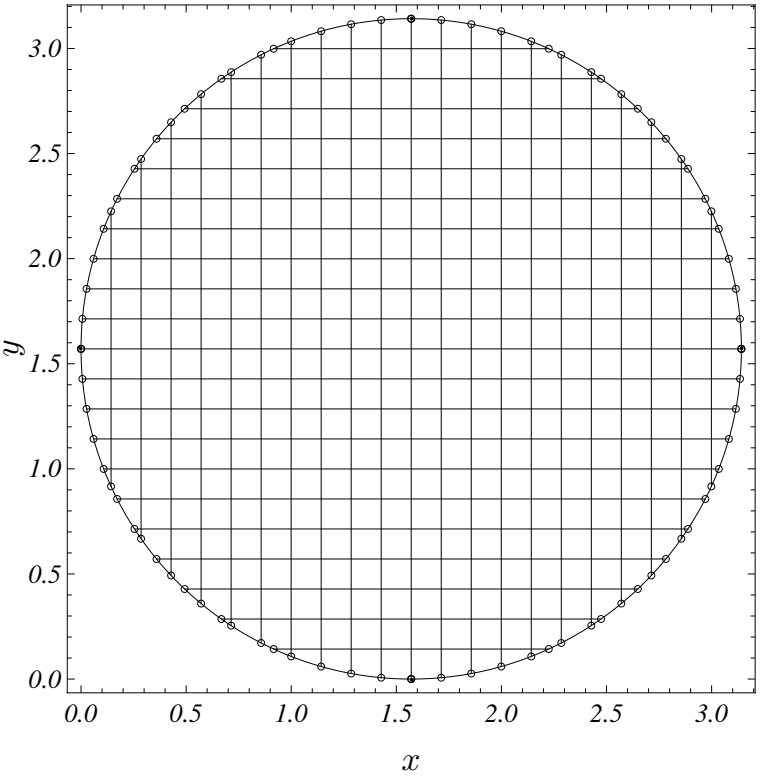

Figure 18: PDE, Problem 2: Geometry and discretisation. Boundary nodes denoted by ∘ are generated by the intersection of the grid lines and the boundary.

$\partial\phi/\partial y$ for the two types of domains are all greater than 2. It can be seen that the proposed technique is able to work well not only for rectangular domains but also for non-rectangular domains.

5 Concluding remarks

In this paper, a new Cartesian-grid-based control-volume technique is proposed for the solution of second-order elliptic problems in one and two dimensions. Integrated RBFs are utilised to construct the approximations for the field variable and its derivatives, which are based on two-node elements and expressed in terms of nodal values of the field variable and its first-order partial derivatives. Various strategies for the imposition of boundary conditions are presented. The proposed control-volume method leads to a system matrix that is sparse and produces a solu-

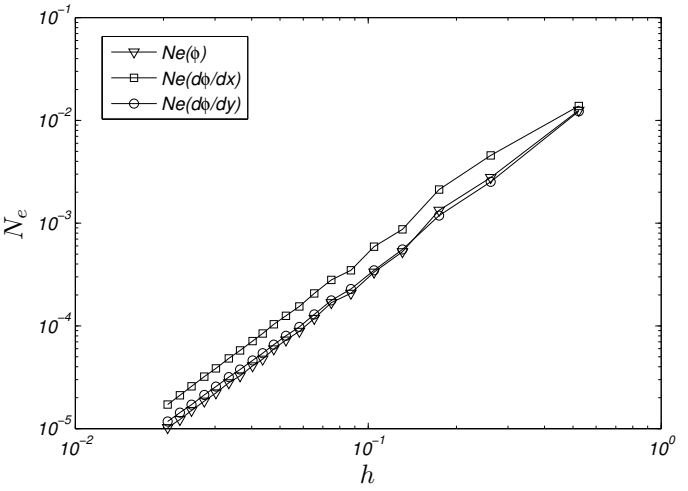

Figure 19: PDE, Problem 2, circular domain, Dirichlet boundary conditions: the solution accuracy using the *D1-D1* strategy and $\beta = 15$.

tion that is C^2-continuous on the grid lines. Its solution accuracy can be effectively controlled by means of the shape parameter (β up to 85) and/or grid size. A series of test problems including those defined on non-rectangular domains are employed to validate the present method. Numerical results show that the method is much more accurate and faster convergence, especially for the approximation of derivatives, than the standard control volume method.

Acknowledgement: D.-A. An-Vo would like to thank USQ, FoES and CESRC for a PhD scholarship. This research is supported by the Australian Research Council.

References

Atluri, S. N.; Han, Z. D.; Rajendran, A. M. (2004): A new implementation of the meshless finite volume method, through the MLPG "mixed" approach. *CMES: Computer Modeling in Engineering and Sciences*, vol. 6, pp. 491–514.

Cheng, A. H. D.; Golberg, M. A.; Kansa, E. J.; Zammito, G. (2003): Exponential convergence and h-c multiquadric collocation method for partial differential equations. *Numerical Methods for Partial Differential Equations*, vol. 19, pp. 571–594.

Divo, E.; Kassab, A. J. (2007): An efficient localized radial basis function meshless method for fluid flow and conjugate heat transfer. *Journal of Heat Transfer*, vol. 129, pp. 124–136.

Fasshauer, G. E. (2007): *Meshfree approximation methods with Matlab*. Interdisciplinary mathematical sciences, vol. 6. Singapore: World Scientific Publishers.

Fedoseyev, A. I.; Friedman, M. J.; Kansa, E. J. (2002): Improved multiquadric method for elliptic partial differential equations via PDE collocation on the boundary. *Computers and Mathematics with Applications*, vol. 43, pp. 439–455.

Franke, R. (1982): Scattered data interpolation: tests of some methods. *Mathematics of Computation*, vol. 38, pp. 182–200.

Ho-Minh, D.; Mai-Duy, N.; Tran-Cong, T. (2009): A Galerkin-RBF approach for the streamfunction-vorticity-temperature formulation of natural convection in 2D enclosured domains. *CMES: Computer Modeling in Engineering and Sciences*, vol. 44, pp. 219–248.

Kansa, E. J. (1990): Multiquadrics-a scattered data approximation scheme with applications to computational fluid-dynamics-II. *Computers and Mathematics with Applications*, vol. 19, pp. 147–161.

Le-Cao, K.; Mai-Duy, N.; Tran-Cong, T. (2009): An effective intergrated-RBFN Cartesian-grid discretization for the stream function-vorticity-temperature formulation in nonrectangular domains. *Numerical Heat Transfer, Part B: Fundamentals*, vol. 55, pp. 480 – 502.

Lee, C. K.; Liu, X.; Fan, S. C. (2003): Local multiquadric approximation for solving boundary value problems. *Computational Mechanics*, vol. 30, pp. 396–409.

Li, J.; Hon, Y. C. (2004): Domain decomposition for radial basis meshless methods. *Numerical Methods for Partial Differential Equations*, vol. 20, pp. 450–462.

Libre, N. A.; Emdadi, A.; Kansa, E. J.; Rahimian, M.; Shekarchi, M. (2008): A stabilized RBF collocation scheme for Neumann type boundary value problems. *CMES: Computer Modeling in Engineering and Sciences*, vol. 24, pp. 61–80.

Madych, W. R. (1992): Miscellaneous error bounds for multiquadric and related interpolators. *Computers and Mathematics with Applications*, vol. 24, pp. 121–138.

Mai-Duy, N.; Le-Cao, K.; Tran-Cong, T. (2008): A Cartesian grid technique based on one-dimensional integrated radial basis function networks for natural convection in concentric annuli. *International Journal for Numerical Methods in Fluids*, vol. 57, pp. 1709–1730.

Mai-Duy, N.; Tran-Cong, T. (2001): Numerical solution of differential equations using multiquadric radial basis function networks. *Neural Networks*, vol. 14, pp. 185–199.

Mai-Duy, N.; Tran-Cong, T. (2003): Approximation of function and its derivatives using radial basis function network methods. *Applied Mathematical Modelling*, vol. 27, pp. 197–220.

Mai-Duy, N.; Tran-Cong, T. (2007): A Cartesian-grid collocation method based on radial-basis-function networks for solving PDEs in irregular domains. *Numerical Methods for Partial Differential Equations*, vol. 23, pp. 1192–1210.

Mai-Duy, N.; Tran-Cong, T. (2008): A multidomain integrated-radial-basis-function collocation method for elliptic problems. *Numerical Methods for Partial Differential Equations*, vol. 24, pp. 1301–1320.

Mai-Duy, N.; Tran-Cong, T. (2009): A Cartesian-grid discretisation scheme based on local integrated RBFNs for two-dimensional elliptic problems. *CMES: Computer Modeling in Engineering and Sciences*, vol. 51, pp. 213–238.

Mai-Duy, N.; Tran-Cong, T. (2010): A control volume technique based on integrated RBFNs for the convection-diffusion equation. *Numerical Methods for Partial Differential Equations*, vol. 26, pp. 426–447.

Mohammadi, M. H. (2008): Stabilized meshless local Petrov-Galerkin (MLPG) method for incompressible viscous fluid flows. *CMES: Computer Modeling in Engineering and Sciences*, vol. 29, pp. 75–94.

Ngo-Cong, D.; Mai-Duy, N.; Karunasena, W.; Tran-Cong, T. (2011): Free vibration analysis of laminated composite plates based on FSDT using one-dimensional IRBFN method. *Computers and Structures*, vol. 89, pp. 1–13.

Orsini, P.; Power, H.; Morvan, H. (2008): Improving volume element methods by meshless radial basis function techniques. *CMES: Computer Modeling in Engineering and Sciences*, vol. 23, pp. 187–208.

Patankar, S. V. (1980): *Numerical heat transfer and fluid flow*. Taylor & Francis.

Sanyasiraju, Y. V. S. S.; Chandhini, G. (2008): Local radial basis function based gridfree scheme for unsteady incompressible viscous flows. *Journal of Computational Physics*, vol. 227, pp. 8922–8948.

Sarler, B. (2005): A radial basis function collocation approach in computational fluid dynamics. *CMES: Computer Modeling in Engineering and Sciences*, vol. 7, pp. 185–194.

Sellountos, E. J.; Sequeira, A. (2008): A hydrid multi-region BEM/LBIE-RBF velocity-vorticity scheme for the two-dimensional Navier-Stokes equations. *CMES: Computer Modeling in Engineering and Sciences*, vol. 23, pp. 127–148.

Shu, C.; Ding, H.; Yeo, K. S. (2003): Local radial basis function-based differential quadrature method and its application to solve two-dimensional incompressible Navier-Stokes equations. *Computer Methods in Applied Mechanics and Engineering*, vol. 192, pp. 941–954.

Tolstykh, A. I.; Shirobokov, D. A. (2003): On using radial basis functions in "finite difference mode" with applications to elasticity problems. *Computational Mechanics*, vol. 33, pp. 68–79.

Šarler, B.; Vertnik, R. (2006): Meshfree explicit local radial basis function collocation method for diffusion problems. *Computers and Mathematics with Applications*, vol. 51, pp. 1269–1282.

Zerroukat, M.; Power, H.; Chen, C. S. (1998): A numerical method for heat transfer probems using collocation and radial basis functions. *International Journal for Numerical Methods in Engineering*, vol. 42, pp. 1263–1278.